



HAL
open science

Influence of inclusion rigidity on shrinkage induced micro-cracking of cementitious materials

Ling Li, Yudan Jin, Yun Jia, Thomas Rougelot, Nicolas Burlion, Jian-Fu Shao

► **To cite this version:**

Ling Li, Yudan Jin, Yun Jia, Thomas Rougelot, Nicolas Burlion, et al.. Influence of inclusion rigidity on shrinkage induced micro-cracking of cementitious materials. *Cement and Concrete Composites*, 2020, 114, pp.103773. 10.1016/j.cemconcomp.2020.103773 . hal-02942597

HAL Id: hal-02942597

<https://hal.science/hal-02942597>

Submitted on 22 Aug 2022

HAL is a multi-disciplinary open access archive for the deposit and dissemination of scientific research documents, whether they are published or not. The documents may come from teaching and research institutions in France or abroad, or from public or private research centers.

L'archive ouverte pluridisciplinaire **HAL**, est destinée au dépôt et à la diffusion de documents scientifiques de niveau recherche, publiés ou non, émanant des établissements d'enseignement et de recherche français ou étrangers, des laboratoires publics ou privés.



Distributed under a Creative Commons Attribution - NonCommercial 4.0 International License

Influence of inclusion rigidity on shrinkage induced micro-cracking of cementitious materials

Ling LI^{a,b}, Yudan JIN^b, Yun JIA^{b,*}, Thomas ROUGELOT^b, Nicolas BURLION^b, Jianfu SHAO^{b,*}

^a*Nanchang Institut of Technology, School of Hydraulic and Ecological Engineering, 330099 Nanchang, China*

^b*Univ. Lille, CNRS, Centrale Lille, UMR 9013 - LaMcube - Laboratoire de Mécanique, Multiphysique, Multi-échelle, F-59000 Lille, France*

Abstract

This paper presents an experimental study on the influence of inclusion rigidity on the shrinkage cracking in a concrete composite. For this purpose, a series of concrete samples are casted with artificial inclusions of different rigidities. These samples are subjected to different levels of drying in order to evaluate cracks induced by the drying shrinkage. The dried samples are then examined by using the non-destructive X-ray micro-tomography imaging method. Three-dimensional (3D) distributions of induced cracks in the dried samples are identified, including their location and shape. The influence of inclusion rigidity on the shrinkage-induced cracking process is clearly demonstrated. It is found that the shrinkage-induced cracking is strongly enhanced by the stiffness difference between the inclusion and cement paste. The experimental results obtained in this study allow to improving understanding of the mechanism of shrinkage cracking in concrete composites.

Keywords: Shrinkage, Drying, Concrete composites, Cracking, Inclusion rigidity, X-ray micro-tomography

1. Introduction

Concrete materials are widely used in different kinds of engineering structures. When they are exposed to a low relative humidity, micro-cracks and fracture are created due to the inhomogeneous desiccation shrinkage of constituent components. In general, due to hydric gradient, the surface area shrinks faster than the internal zone and a non-uniform shrinkage process is generated in a concrete body. Consequently, surface cracks are widely observed at the macroscopic scale in many concrete structures [2, 15]. At the scale of aggregates, micro-cracks are generated due to the fact that the shrinkage of cement paste is constrained by the stiff inclusions [14]. As a result, hydro-mechanical properties of concrete materials can be significantly affected [3, 27], for instance, the decrease of elastic modulus and mechanical

*Corresponding authors: yun.jia@polytech-lille.fr, jian-fu.shao@polytech-lille.fr

11 strength and the increase of permeability. Therefore, a large number of studies have been
12 performed to investigate different influences of inclusions (aggregates) on the drying cracking
13 process of concrete composites, including inclusion size and volume fraction [12] and others.
14 To the best knowledge of authors, the influence of inclusion rigidity on the shrinkage cracking
15 has not been widely studied in experimental investigations. This is partially due to the
16 difficulty of getting a 3D cartography of cracks without modifying the microstructure of the
17 sample and selecting inclusions compatible with the imaging technique. The main objective
18 of the present study is then to investigate the influence of inclusion rigidity on the shrinkage
19 cracking in concrete composites by using a non-destructive laboratory testing method.

20 In order to visualize the evolution of microstructure, different types of techniques have
21 been developed, for instance, acoustic emission measurement [23], infrared thermography,
22 impregnating florescence microscopy [4] and environmental scanning electron microscope [4].
23 Each technique has different advantages and shortcomings. The environmental scanning
24 electron microscope is generally limited to regions very close to the surface of sample and
25 more suitable for the small-scale observation of fine micro-structure such as morphology
26 and mineral compositions. The method with a fluorescent epoxy impregnation also has
27 limitation in observation depth from the surface of sample. The acoustic emission is more
28 suitable to detect the appearance of cracks and widely combined with other methods [1].
29 In addition, some of those techniques are destructive and can lead to secondary micro-
30 cracks. With the development of imaging technology and computer processing, the X-ray
31 computed micro-tomography (XCMT) becomes a very powerful non-destructive monitoring
32 technique. This technique is able to provide high resolution images to capture the evolution
33 of micro-structure and can be easily combined with in-situ mechanical tests. It has been
34 widely used for cement based materials for the identification of micro-structure [20, 10,
35 17], the characterization of induced micro-cracks under different loading conditions [17, 9],
36 the micro-structural degradation during chemical leaching [6, 22], and the drying cracking
37 [25], etc. The XCMT imaging technique provides 3D full-field visualization and very rich
38 information on the material micro-structure, such as crack shape, size and distribution. In
39 the present study, the XCMT technique will be used to characterize the drying shrinkage
40 cracks developed in concrete composites with different types of inclusions (aggregates). The
41 emphasis is put on the effect of inclusion stiffness or rigidity on the process of drying shrinkage
42 induced micro-cracking. A series of concrete samples are fabricated by using different kinds
43 of artificial inclusions of different rigidities. These samples are subjected to different levels of
44 drying in order to create shrinkage-induced cracks. High resolution X-ray micro-tomographic
45 images are taken from the cracked samples. The three-dimensional patterns of shrinkage-
46 induced cracks are established and compared between the different samples. The influence
47 of inclusion rigidity on the cracking patterns is analyzed and discussed.

48 The present paper is organized as follows. The sample preparation procedure, experi-
49 mental device and testing program are first presented. Qualitative results on the shrinkage-
50 induced cracks patterns are then shown. The identification and quantification of the crack
51 networks are finally presented.

2. Sample preparation and experimental program

In concrete, due to the great variability of inclusions (i.e. shape, size, distribution and porosity, etc.) and the eventual reaction between cement matrix and inclusion, it is very difficult to analyze the mechanisms controlling the creation and development of cracks. For the sake of simplification and considering the idea initially proposed by Bisschop and van Mier [23], the present work is performed on a cementitious composite made with a 40% volume fraction of spherical inclusions and a 60% volume fraction of cement paste. This type of composite allows us to study a simplified cementitious composite, in which spherical inclusions are distributed in a mono-disperse manner.

2.1. Sample preparation

Firstly, the influence of inclusion rigidity on the shrinkage cracks is experimentally studied. In order to better achieve a micro-tomographic imaging and taking advantage of the difference of X-ray attenuation coefficient between cement paste matrix and inclusions, five types of cementitious composites have been formulated by using five different materials as inclusions: Titanium, Zirconium, Glass, Polyamide and polyoxymethylene (Fig.1). These five spherical inclusions have a smooth, rounded surface with the objective of minimizing the bonds at the interfaces between cement paste and inclusions. The diameter of inclusions is $2mm$ so that the opening of cracks is sufficient to be detectable at the available resolution (see the previous work in [19]). It should be noticed that the volume fraction of inclusions is 40% in each composite. In order to fit the field of view of camera used in the micro-tomographic imaging, the cylindrical samples is selected to be $8mm$ in diameter and $15mm$ in height. A typical CEM I 52.5 cement is used according to the European standards. A W/C ratio of 0.5 is adopted and this ratio is capable of ensuring a casting without requesting strong vibration. For each type of cementitious composites, one sample is casted and conserved in lime saturated solution under $20^{\circ}C$ for more than one month. For the sake of convenience, all the samples are labelled with respect to the type and stiffness of inclusions (for instance: Zr-200 for Zirconium with a Young's modulus of 200GPa). The main properties of inclusions (density, Young's modulus, Poisson's ratio, hardness, thermal dilatation coefficient and hydric properties) are given in Table 1. And the linear thermal expansion coefficient of the cement paste used in this study is about $10 \times 10^{-6}/^{\circ}K$ [7].

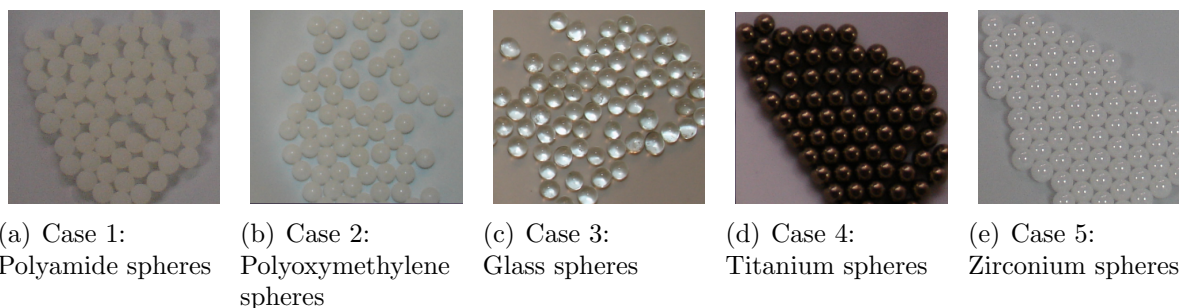


Figure 1: Different types of inclusions used in this study

	Case1	Case2	Case3	Case4	Case5
Materials	Polyamide 6.6	Polyoxymethylene	Glass	Titanium	Zirconium
Density (g/cm^3)	<u>1.14</u>	<u>1.40</u>	<u>2.50</u>	<u>4.45</u>	<u>6.05</u>
Young's modulus (GPa)	1.70-2.00	2.40-2.80	<u>68</u>	112	<u>200</u>
Hardness**	<u>100D</u>	<u>80D</u>	<u>465-585HK</u>	<u>28-42HRC</u>	1100HV
	78-121HRR	69-121HRR	450-550HV	290-420HV	
	85-180MPa BIH	30-179MPa BIH			
Linear thermal expansion coefficient ($10^{-6}/^{\circ}K$)	70-100	80-100	<u>9.6</u>	8.9	<u>10</u>
Thermal conduc- tivity ($W.m^{-1}.K^{-1}$)	0.2-0.3	0.2-0.31	<u>1</u>	16	<u>2</u>
Water ab- sorption	2-4%	0.25%	-	-	-
Poisson's ratio	0.38-0.45	0.35-0.43	0.17-0.25	0.26-0.34	0.23-0.32

Table 1: Parameters for different materials of inclusions*

* The underlined values are provided by the material production company, the others are obtained from literature review.

** Hardness Knoop (HK); Hardness Shore Durometer (D); Hardness Vickers (HV); Hardness Brinell (HB); Hardness Rockwell (HR); Ball Indentation Hardness (BIH). These methods are used for different kinds of materials. There are no direct and unique conversion formula between them, only some empirical relations.

82 2.2. Drying procedure and micro-tomographic acquisition

83 All the samples are firstly conserved in a lime saturated solution at a temperature of
84 around 20°C to ensure the maturation of the cementitious matrix and a full water saturation
85 of samples. As under a small hydric gradient, the drying cracking may not be very obvious

86 and the detection of fine cracks will be very difficult, two successive drying steps are used
 87 here respectively with a large variation of relative humidity and temperature.

88 In the first step, the relative humidity (RH) is reduced to 12% under a temperature (T)
 89 of 20°C and maintained for about 30 days until the mass stabilization of samples. Then a
 90 seconde drying step is performed by increasing the temperature to 105°C and maintaining
 91 it for about 20 days. The two step are designed in order to achieve a dry state of samples
 92 with a limited modification of the hydrate structure. The two drying steps are realized
 93 in a Vötsch® or Binder® climatic chamber allowing a continuous control of the values of
 94 temperature and relative humidity. The weight of samples is measured by using a balance
 95 with a precision of $\pm 0.01\text{g}$. When the weight variation of a sample is less than 0.1% during
 96 7 days, the desired drying state is supposed to be obtained. As the volumetric densities of
 97 five types of inclusions are different, a normalized weight loss of the cementitious matrix is
 98 calculated by assuming no mass loss of inclusions. This assumption can be too strong in
 99 the case 1 (Pam-2) because the water absorption of Pam-2 is not null during drying process.
 100 The obtained values of normalized mass loss for five types of samples are given in Fig.2.

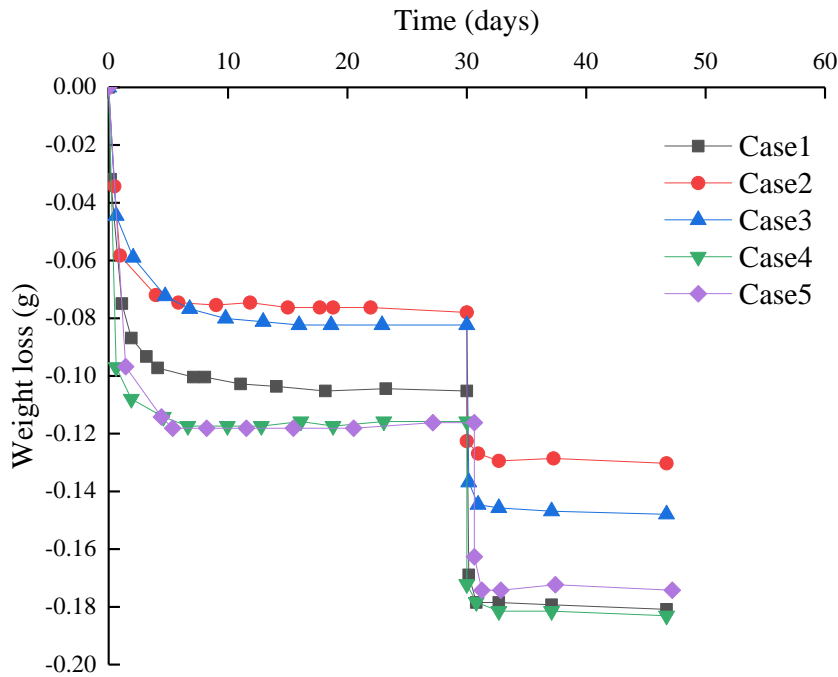


Figure 2: Evolution of normalized weight loss of five types of samples with drying time

101 The microstructural evolutions of dried samples are analysed with the help of X-ray
 102 micro-tomographic imaging technique. For this purpose, images are taken at the initial
 103 saturated state, at the end of the first step of drying and at the end of the second step
 104 of drying. At the end of the first step, there is an increase of temperature from 20°C to
 105 105°C. Due to the difference of thermal expansion coefficient between the cement paste and
 106 different inclusions, the temperature increase can generate important cracks in the samples.

107 It would be ideal to take micro-tomographic images just after the temperature is increased.
108 Therefore, only the micro-tomographic images at three moments are taken and analyzed in
109 this study. More precisely, for the inclusions case1 and case2 used in this study (see Table 1),
110 their thermal expansion coefficients are clearly higher than that of the cement paste (about
111 10 times). The thermal expansion induced cracking can be an important process for these
112 two composites. However, for the other three types of inclusion, the difference of thermal
113 expansion between the inclusions and the cement paste is very small. The thermal expansion
114 induced cracking process should be less significant. However, more detailed investigations
115 should be performed in future works.

116 The micro-tomographic acquisition is carried out by using the ISIS4D platform [21] as
117 shown in Fig. 3. The X-Ray beam is produced by a micro-focus X-ray tube with a tension of
118 100kV for the case4 (Ti-112) and 80kV for the other cases. To reduce the signal interference
119 by beam hardening [5], a aluminium filter with a thickness of 0.1mm is adhered to the source.
120 The flat panel detector has a resolution of 1920×1536 pixels. Helicoïdal acquisition is used
121 and allows us to scan the entire height of studied samples. The number of radiographies
122 for each sample is 4320. The procedure for a tomographic scan is illustrated in Fig.4. The
123 resolution of the XCMT imaging used here is about 7 μm . For the sake of simplicity and
124 based on some previous studies [18, 8], the voxel size is assumed to approximately equal
125 to the resolution of the instrument, that is 7 μm . As a consequence, cracks with a width
126 smaller than this value are not detected while cracks with a width entre 7 μm and 14 μm are
127 also difficult to identify.

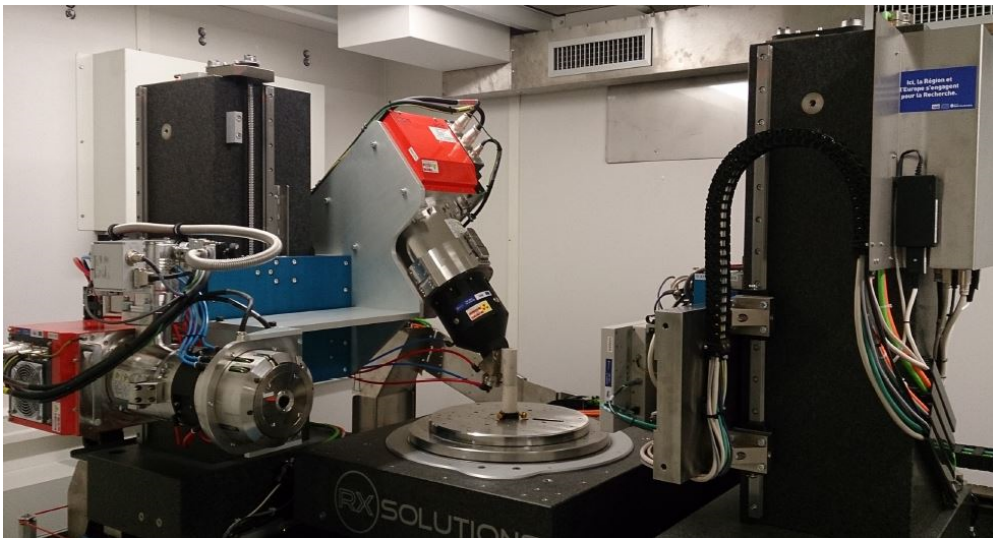


Figure 3: The micro-tomography equipment (platform ISIS4D)

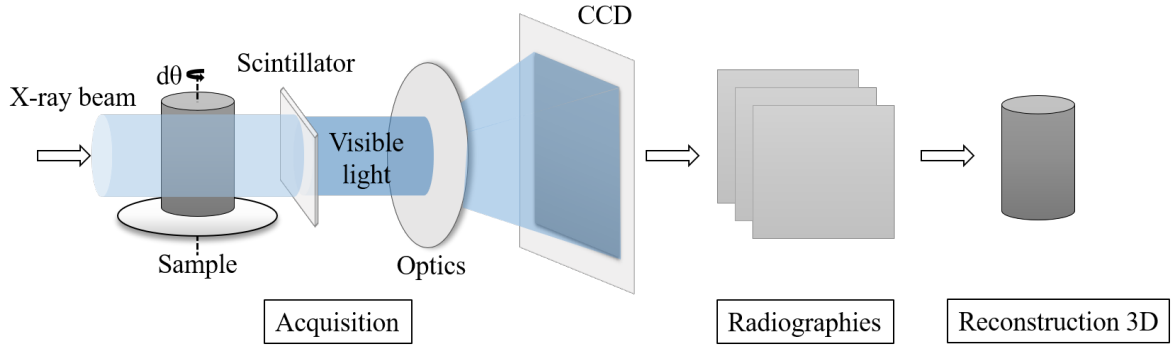


Figure 4: Sketch of acquisition and reconstruction of micro-tomographic images

128 2.3. Image processing method

129 In order to obtain reliable reconstructed images from the experimental analysis, some
 130 treatments are used to reduce the inherent defects or artifacts in the acquisition technique.
 131 Some preventive measures are also considered to avoid the aliasing, for example, using
 132 appropriate sampling frequency, detector and number of projections, etc. In the present
 133 study, the acquisition with helicoidal mode, the polychromaticity of X-ray will cause the
 134 beam hardening phenomenon [5]. For the purpose to reduce the coupling artifacts of beam
 135 hardening, in combination of the aluminium filter adhered to the source, a procedure for
 136 adjusting attenuation curves [13] is adopted by readjustment of the polynomial curve.

137 Based on the reconstructed 3D volume, the cracks networks developed in the samples are
 138 identified, visualized and quantified. The image segmentation is obtained by using the grey
 139 values of every voxel. The obtained measuring results are the volume and surface of cracks.
 140 The volume is equal to the multiplication of the number of voxels in the porous phase and
 141 the elementary volume of a voxel (a^3). The surface corresponds to the multiplication of
 142 voxel numbers of facets and the area of a facet (a^2) in the porous phase which are in contact
 143 with the solid phase. In practice, the volume changes is presented by the number of counted
 144 voxel while the surface is described by the number of detected pixels.

145 In this study, the experimental observations of a selected cross-section are compared
 146 between the three scanning states (the initial state, the end of the step 1 and the end of
 147 the step 2). For each acquisition, it is difficult to place the sample in the same position.
 148 Moreover, due to the fact that the sample may not be placed absolutely vertically, a rotation
 149 angle is necessary. Consequently, the presentation of studied cross-section may be a little
 150 different for three acquisition moments. In view of this, an image registration is realized on
 151 the reconstructed images. Totally, two reconstructed volumes of each studied sample are
 152 registered by the way of rigid transformation based on the geometric characteristics i.e. the
 153 positions of the beads or cement paste.

154 As the samples are initially saturated and then dried, the compositions of sample may
 155 be modified due to the moisture change. As a result, the attenuation coefficient of the same
 156 sample may be slightly different between the different moments. This change is observed as
 157 the displacement of the grey level in the histogram. Therefore, the calibration of histogram

158 allows us to acquire the useful information with the same threshold. Characteristics of
159 the image can be enhanced in order to help segmentation of cracks by applying filters: a
160 median filter and an anisotropic diffusion filter will be used in this study [26, 16]. After
161 these treatments, the surface and volume measurements will be less sensitive to the selected
162 threshold values.

163 **3. First qualitative results of cracking patterns**

164 The main experimental results obtained on five types of samples are presented in this
165 section. In order to illustrate the influence of inclusion rigidity on the shrinkage cracks of
166 cementitious composites, the experimental results of saturated states and different drying
167 steps are compared and analysed. The debonding of interfaces between the cementitious
168 matrix and inclusions can also be clearly seen for the cases 4 and 5.

169 The micro-tomographic acquisitions will be able to more deeply investigate the effect
170 of drying on those samples. In Table 2, one shows the selected cross-sections (around the
171 mid-height of samples) inside the samples for the different drying steps. Due to their small
172 sizes and the presence of inclusions, the studied samples are very fragile. With the presence
173 of drying induced cracks, they become more fragile. Therefore, some samples are broken into
174 pieces and then the sample scan becomes more difficult. The superficial cracks observed in
175 samples after the last step of drying (105°C) are shown in Fig.5. Except for the case 2 (Pom-
176 3), almost no surface cracks are observed in the cases with a small value of Young's modulus
177 (for instance case 1 (Pam-2)). However, the cracks become more and more numerous with
178 the increase of inclusion stiffness (one large crack in case 3 (Gl-68), lots of cracks for cases
179 4(Ti-112) and 5(Zr-200)).

180 The initial saturated samples are firstly compared. In general, no cracks are visible in the
181 samples except the sample with polyamide spheres (case 1:Pam-2). When the samples are
182 saturated, two types of initial pore voids can be observed: one is air bubbles and relatively
183 large and varied width strips; another is located around the spheres or in the matrix. Most
184 of these void extend in the horizontal direction due to the unsatisfactory filling in the prepa-
185 ration process of samples. On the other hand, some cracks are observed in the saturated
186 samples with polyamide spheres (case 1: Pam-2) and often located around the spheres and
187 in a radial direction around inclusions. These cracks may be related to the water absorption
188 of Pam, which induces the expansion of inclusions at early age.

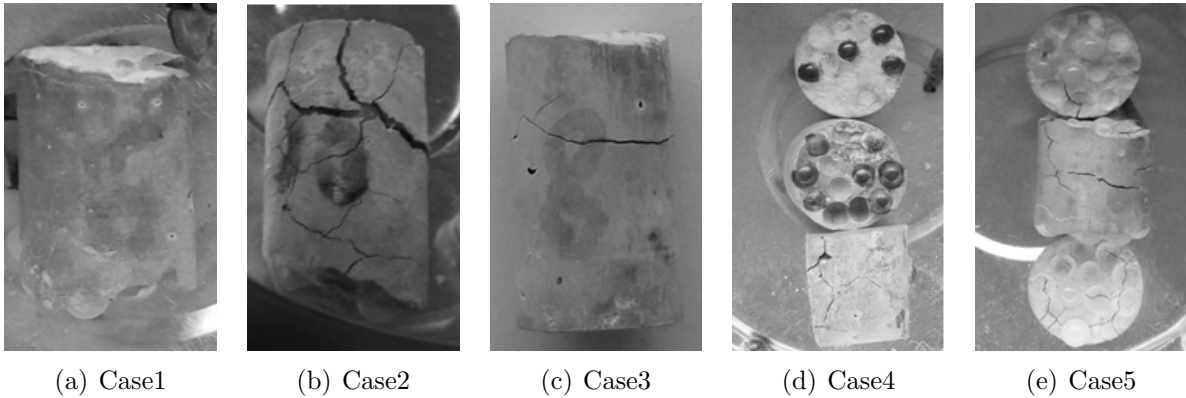


Figure 5: Images of different samples at the end of second drying step at 105°C

189 The different components can be visually distinguished according to the obtained X-
 190 ray attenuation: the weaker the attenuation, the darker colour the figure presents. As a
 191 darker color indicates a low density of material, anhydrous cement grains is presented in
 192 the form of very white spots while air bubbles appear in the form of dark circles. More-
 193 over, crystal portlandite is sometimes presented within them. The spheres appear as circles
 194 with the gray level more homogeneous than the cement paste. Some small dark circles
 195 inside the polymeric spheres reflect the defects of spheres. The attenuation coefficients
 196 for different spheres are quite different and classed as following (from small to big): poly-
 197 oxymethylene, polyamide, glass, Titanium spheres and Zirconium. It should be noted that the
 198 acquisition micro-tomographic doesn't work for the samples with Zirconium spheres because
 199 of its strong attenuation coefficient and apparition of artifacts due to this strong X-ray atten-
 200 uation contrast. The different constituents of concrete composites are visually distinguished
 201 through their X-ray attenuation. In general, when the attenuation is weaker, the color of
 202 obtained images is darker, and vice versa. In the case with Zirconium inclusions, due to their
 203 X-ray strong attenuation, the inclusions and the cement paste have a high contrast between
 204 their images. This high contrast makes that the inclusions have a high brightness and light
 205 color while the cement paste is close to black color. This makes it very difficult to distinguish
 206 cracks from the cement paste. More precisely, in Table 2, one can observe that for the case 4
 207 the cement paste and cracks are both indicated by a very close gray color. Therefore, cracks
 208 in this kind of composite is hardly detectable with the present micro-tomographic technique.

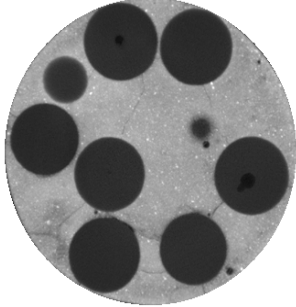
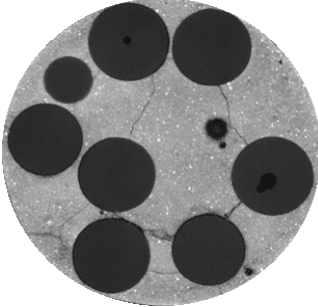
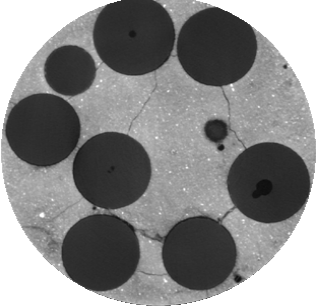
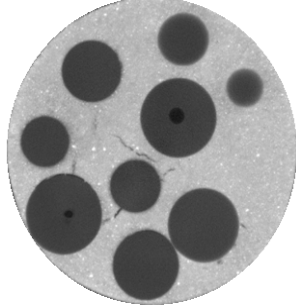
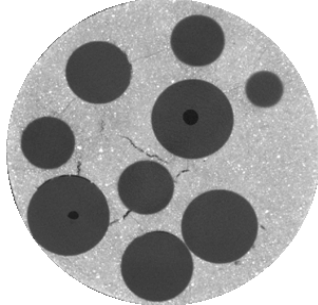
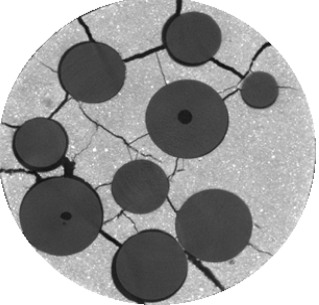
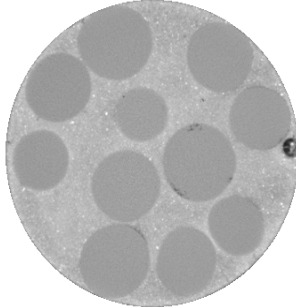
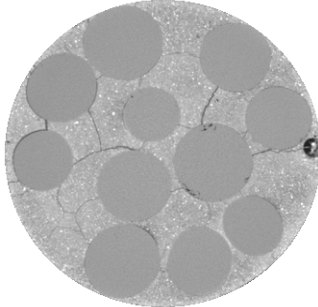
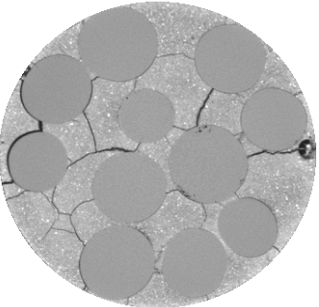
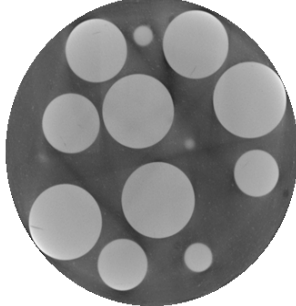
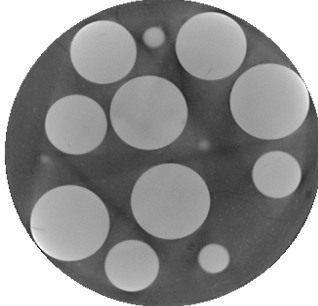
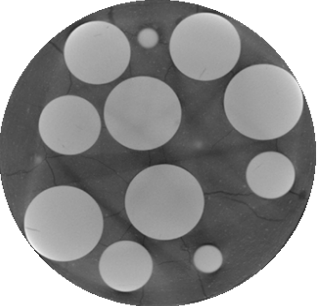
	Saturated (T = 20°C)	Drying, end of step 1 (T=20°C HR=12%)	Drying, end of step 2 (T=105°C)
Case1 (Pam-2)			
Case2 (Pom-3)			
Case3 (GI-68)			
Case4 (Ti-112)			

Table 2: Reconstructed images of representative cross-section in different samples et different steps of drying

209 After the first phase of the drying process, no obvious cracks are observed in the case 2
210 (samples with polyoxymethylene spheres). Conversely, some very fine cracks begin to appear
211 in the sample with Titanium spheres (case 3) mainly around the inclusions or between them.
212 However, these cracks are too thin to be seen clearly due to the fact that gray values are
213 very close to that of surrounding material. In the case with other spheres (cases 4 and 5),
214 cracks are more obviously developed than the case 3 but a similar distribution pattern is
215 observed. At the end of the second drying step, wider and longer cracks appear in all the
216 samples and some of them join to each other. It is observed that cracks are significantly
217 created during the second drying step. When these samples are heated to 105°C and the
218 dried at this temperature, the cracks width increases obviously. However, it is important to
219 point out that the physical mechanisms of cracking during the second step are complex [24].
220 Cracks are generated by both the thermal expansion and hydric drying. In particular, for
221 the cases 1 and 2, the thermal expansion coefficients of inclusions are about 10 times higher
222 than that of the cement paste which is about $10^{-5}/^{\circ}C$. This large difference of thermal
223 expansion between the inclusions and cement paste can generate important tensile radial
224 stresses around the inclusions leading the creation of radial cracks. As no XCMT images
225 are taken just after the heating, it is not possible to distinguish the cracked induced by
226 the thermal expansion from those by drying process. However, for the other samples, for
227 instance the case 3, the difference of thermal expansion is very small between the inclusions
228 and cement paste, it seems reasonable to assume that the drying cracking is the principal
229 process during the second step. The cracks shown in Table 2 for the case 3 are mainly
230 created by the drying shrinkage of the cement paste.

231 Indeed, by assuming that no water is present inside the inclusions, the drying steps
232 leads to the decrease of waste content in the cement paste. The desaturation induced the
233 volumetric shrinkage of cement paste. Due to presence of inclusions with a higher stiffness
234 than that of the cement paste, the free shrinkage of the cement paste is restrained. This
235 will generate a stress concentration around the inclusions and the creation of cracks. In the
236 case of spherical particles, tensile tangential and compressive radial stresses are generally
237 generated around the inclusions. The tensile tangential stress leads to the nucleation and
238 propagation of radial cracks (see Table 2). In case of non-spherical inclusions, more complex
239 cracking patterns can be obtained. Moreover, the amplitude of tensile stress depends on
240 the difference of stiffness between the cement paste and inclusions. When the inclusions are
241 much stiffer than the cement paste, a high tangential stress can be generated. In our study,
242 the elastic modulus of inclusions in the case 3 is higher than those in the cases 1 and 2. One
243 can see that the drying induced cracks during the first step are more important for the case
244 3 than for the cases 1 and 2.

245 However, a special attention is paid on the sample with polyamide spheres (case 1).
246 Differently from the other cases (2-4), some cracks are also observed even at the initial
247 saturated state (see Table 1). Moreover, cracks are created at a very early moment during
248 the first drying step. These results may be due to the water absorption ability of polyamide.
249 By comparing the edge of polyamide spheres in two drying steps, it can be noted that
250 the circumferential cracks seem very similar in two step. Additionally, it is verified that
251 the circumferential cracks (i.e. interface debonding between inclusions and matrix) in two

252 drying phases are created by the contraction of spheres, which are due to the water lost and
253 can be measured by the pixels of spheres.

254 By comparing the samples with glass inclusions (case 3) and Titanium spheres (case 4),
255 more circumferential cracks are observed in the sample with glass spheres. This difference
256 should be related to the strong X-ray attenuation coefficient of Titanium spheres, leading to
257 an image of inclusions with high brightness and light color. As a result, the cracks around
258 the inclusions may be hindered.

259 As, mentioned above, due to the technical limitation of the experimental device, no
260 scanned images are taken just after increasing temperature to 105°C. Therefore the effects
261 of differential thermal expansion on the cracking process cannot not be quantified here. As a
262 result, it is not possible to distinguish the thermal expansion induced cracks from the drying
263 induced ones, in particular for the cases 1 and 2. However, for the cases 3, 4, and 5, due to
264 the small difference of thermal expansion between the cement paste and inclusions, we can
265 assume that the thermal expansion effect is relatively small.

266 **4. Identification and quantification of the crack network**

267 The crack network in four types of cementitious composite are compared and analysed
268 in this section. The general procedure of image analysis is firstly presented via a sample with
269 Titanium spheres (case 4). The gray value histograms of case 4 are given in one cross-section
270 (Fig.6). Different phases are represented by the observation of different picks. In order to get
271 a good presentation of cracks, some image filter techniques are used. Median filter reduces
272 the noise and enhances image characteristics while anisotropic diffusion filter homogenize
273 the gray value in each phase. Therefore, the difference between the obtained results of two
274 filters can help to see more clearly the cracks. Meanwhile, the intermediate value at the
275 interface of cement paste and inclusions will also be highlighted. Finally, a filter analysis is
276 done to eliminate the smallest noise, which is assumed as creating connected components and
277 smaller than 100 voxels. The same image analysis has been performed for all the samples.

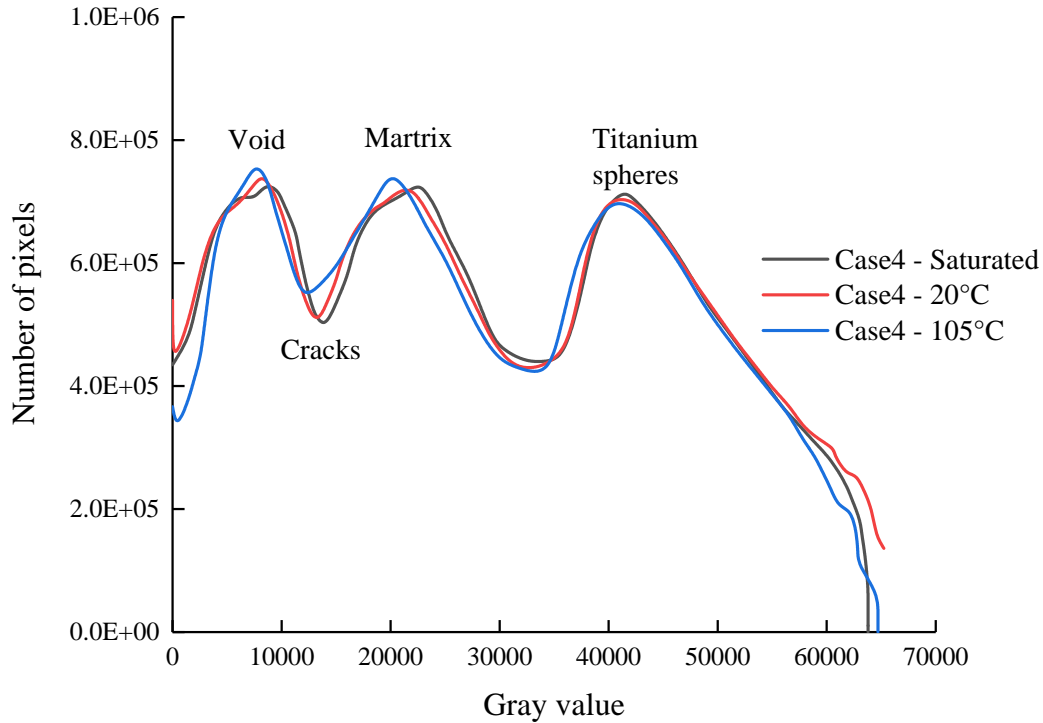


Figure 6: Histogram of one representative cross-section (mid-height) of samples with Titanium spheres

278 By using the image analysis procedure described above, cracks are visualized and detailed
 279 in Table 3. The same color denotes a family of connected cracks. The color assignment is
 280 randomly generated by the image analysis software. One can note that the gray values at
 281 both ends of the specimen are often prone to bias and interference information are more
 282 easily introduced during image segmentation. Moreover, some samples are even broken, in
 283 which only subsets of volume for the cracks detections are used. On the other hand, at the
 284 interface between inclusions and matrix, there are often many intermediate gray values which
 285 are very close to the gray value of cracks. In order to avoid these effects, the edge of spheres
 286 and the spheres are also removed in the final image. As a result, the circumferential cracks
 287 are not included in the samples 3. A refining procedure will be proposed later (avoiding
 288 the use of the additional mask) in order to take into account the circumferential cracks for
 289 suitable composites (glass and polyoxymethylene spheres).

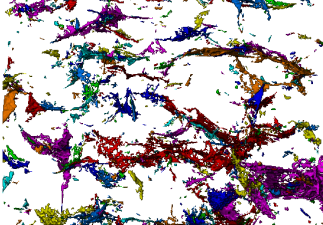
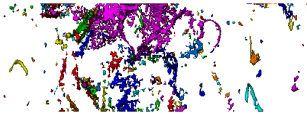
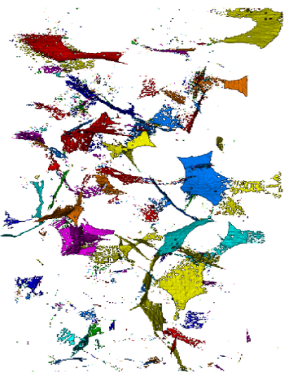
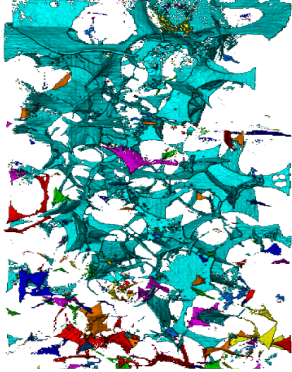
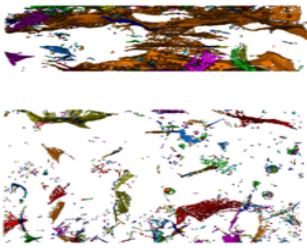
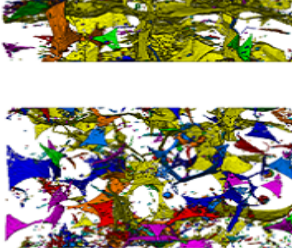
	Initial saturated state ($T = 20^{\circ}\text{C}$)	End of drying step 1 ($T=20^{\circ}\text{C}$, HR=12%)	End of cooling in drying step2 ($T=105^{\circ}\text{C}$)
Case1 (Pam-2)			
Case2 (Pom-3)	No cracks		
Case3 (Gl-68)	No cracks		
Case4 (Ti-112)	No cracks		

Table 3: Evolution of 3D crack network in different samples (each color denotes the same family of connected cracks)

290 In Fig.7, one shows the evolutions of the volume and area of cracks during the two drying
291 steps for 4 concrete composites. The continuous lines represent the cracks excluding the
292 circumferential cracks or debonded interfaces for which an additional mask is applied. For the
293 glass and polyoxymethylene spheres for which a very small number of circumferential cracks

294 and or debonded interfaces is observed, the dashed lines represent all the cracks observed.
 295 Due to the different size of subsets, the quantities of cracks are given in standardized form
 296 (convert to quantities per slice). Again, it should be noted that in the cases 1 and 2,
 297 important radial cracks can be induced the differential thermal expansion during the heating
 298 phase and those thermal cracks cannot be separated from the drying induced ones.

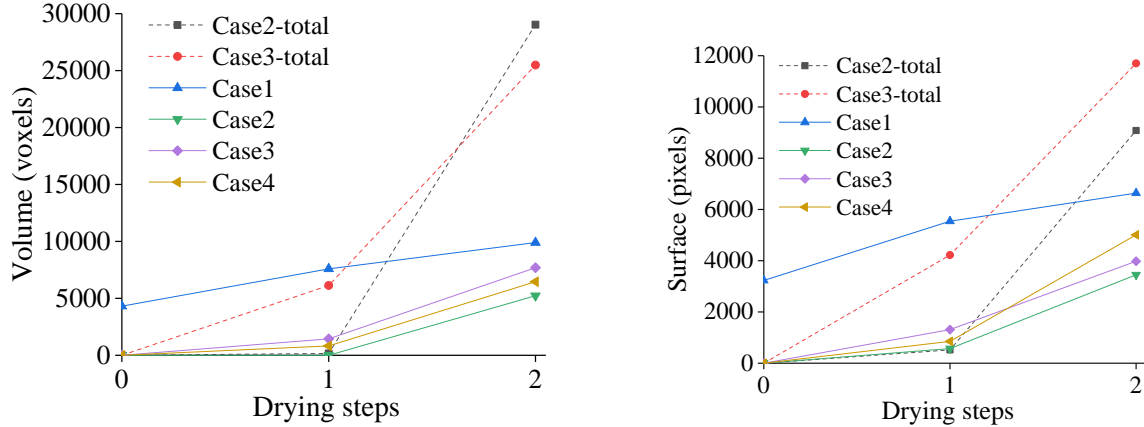


Figure 7: Evolution of the volume and area of crack space with drying steps

299 Only the samples with polyamide spheres have cracks in saturated state. The quantity
 300 of cracks for other samples in saturated state is almost null. The quantization of cracks is
 301 obtained in a relatively large volume, so the result is much more reliable compared to the
 302 qualitative results obtained in only one cross-section or from the surface of sample.

303 The cracks develop progressively with the drying processes in all samples, except for the
 304 samples with polyamide spheres (case 1). By comparing the total cracks with the radial
 305 cracks in glass (case 3) and polyoxymethylene (case 2) composites, it is found that most of
 306 cracks are circumferential cracks. Therefore, it may be possible that such circumferential
 307 cracks also exist in the titanium composite (case 4) and cannot be measured due to artefacts
 308 around inclusions, which are related to the strong contrast in the X-ray absorption coefficient
 309 between titanium and the cementitious matrix. The same evolution tendency are observed
 310 in cracks surface and volume.

311 The evolution of volume and surface of cracks with the Young's modulus is shown in
 312 Fig.8. In this figure, only the results for three types of composites are compared. By
 313 eliminating the impact of temperature on polyoxymethylene spheres (case 2) that expansion
 314 increases more the number of cracks than for other sphere materials (see dilation coefficient
 315 in Table.1), one can see that the total amount of cracks increases with the Young's modulus.
 316 According to the radial cracks, the same evolution tendency is observed while the amplitude
 317 is smaller. By comparing the results of the samples with glass (case 3) and Titanium (case
 318 4) spheres, the total cracks increase with the Young's modulus while the radial cracks are
 319 almost unchanged. As a result, one can conclude that the quantity of radial cracks have a
 320 slight increase with Young's modulus.

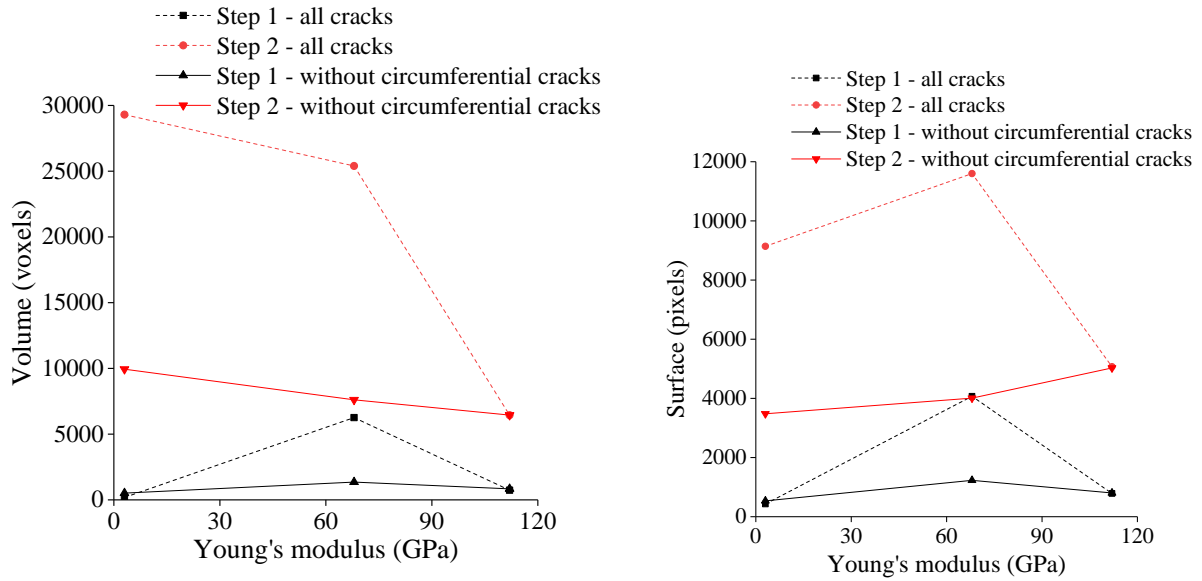


Figure 8: Evolution of the volume and area of crack space with Young's modulus

321 A significant increase in total cracks is observed in the samples with polyoxymethylene
 322 (case 2) and glass (case 3) spheres while no significant increase of cracks are observed in the
 323 sample with Titanium spheres (case 1). These observations can be explained by the following
 324 phenomena:

- 325
- 326 (1) Crack detection is more difficult for samples with Titanium spheres after drying at 20°C
 327 and HR=12% because of the very small width having a few pixels. The difference
 328 of grey level between the cracks and the matrix is not so obvious than that in the
 329 other specimens. The high attenuation coefficient for Titanium spheres generates
 330 beam hardening and may lead to underestimate of circumferential cracks. Moreover,
 331 the debonding of aggregates from a cement paste in drying due to the restriction of
 332 aggregates can probably take place without being visible as an "open" debonding crack.
 333 The radial compressive stress associated with the inclusions restriction may lead to the
 334 closure of debonding cracks that were formed by shearing [11];
 - 335 (2) With a greater Young's modulus, the local effect should be more important. But there
 336 may be an apportionment of cracks around spheres, means cracks become thinner in
 337 width so that they are more difficult to be detected [11];
 - 338 (3) Other parameters for Titanium can also have an additional impact on the cracking,
 339 such as rugosity of the spheres surface.

340 In view of these phenomena, the results for the samples with Titanium spheres is not
 341 representable. In general, the cracks surfaces increase with the Young's modulus under a
 342 strong drying (step 2, T=105°C). Furthermore, some different crack-pattern measurements

343 may be applied to the segmented crack spaces, for instance connected component analysis
 344 and cracks orientation.

345 As a special attention of present study is put on the width and length of cracks, the
 346 measured crack width in different specimens are shown in Fig.9. The largest number of
 347 cracks is concentrated in the range of about 5-6 pixels, which is equal to about 35-42 μm
 348 for all samples. The crack width ranges mainly from about 3 pixels to 30 pixels (about
 349 21-210 μm) for samples with Titanium spheres, polyamide spheres and glass spheres (case 1,
 350 case3-5) while the crack width is expanded to about 60 pixels (420 μm) in the sample with
 351 polyoxymethylene spheres (case 2). Note that the crack width may be a little overestimated
 352 because of the image filter. In addition, some large cracks may be related to the defects
 353 or initial pores. It can be observed that more thin cracks are presented in the sample with
 354 titanium spheres (case 4) than the sample with glass sphere (case 3). An underestimation
 355 of thin cracks in the sample with titanium spheres (case 4) may be more important than the
 356 sample with glass spheres (case 3). The accumulated length of cracks in different samples
 357 is given in Fig.10. It can be seen that this accumulated length of cracks is largely lower
 358 in case 3 than in the case 4. These observations are consistent with an increase number of
 359 thinner cracks in titanium composite and the underestimation of volume of cracks is more
 360 important in the sample with titanium and may explain the discrepancies of resolution of
 361 the X-ray microtomography (Fig.10).

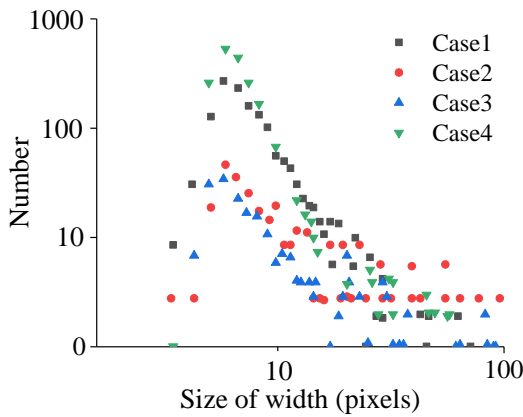


Figure 9: Measured width of cracks in different samples (step 2)

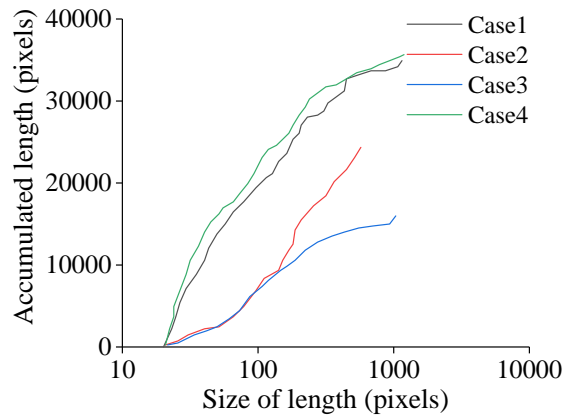


Figure 10: Accumulated length of cracks in different samples (step 2)

362 Base on the experimental investigation, some partial conclusions are taken:

- 363 • X-ray microtomography was able to detect the changes in cracking pattern for different
 364 composites;
- 365 • Several biases may exist in the computation of crack volume and are mainly related
 366 to the images resolution and the cracks detection. Moreover, they may be due to

367 the artifacts, for instance in the composites with a high contrast in X-ray attenuation
368 coefficient between inclusions and cement matrix;

- 369 • In the samples with a higher Young's modulus, a greater increase in the crack surface
370 is observed with an increase of the inclusions' stiffness , specially in the dramatically
371 dried specimens ($T= 105^{\circ}\text{C}$). This observation tends to be confirmed by a greater
372 number of thin cracks and a greater cumulative length of cracks in titanium composite
373 than in glass one.

374 However, due to a number of artifacts and the achievable X-ray imaging resolution, it is
375 difficult to draw the definitive conclusions in terms of the quantitative evolutions of crack
376 characteristics with the rigidity of inclusions. Further studies are still needed.

377 5. Conclusions

378 In the present work, an experimental study has been performed to investigate the in-
379 fluence of inclusion stiffness on drying shrinkage-induced cracking in concrete composites.
380 Based on the obtained results, the following main remarks can be formulated.

- 381 • The cracking process induced by drying shrinkage and heating has been clearly cap-
382 tured by using the X-ray micro-tomographic imaging technique.
- 383 • The experimental results have clearly shown that when the cement paste shrinkage was
384 restrained by the stiffer inclusions, radial cracks were induced and driven by tensile
385 circumferential stresses. Cracks of cement paste between inclusions were also gener-
386 ated due to the strong interactions between inclusions. The drying shrinkage induced
387 cracking was enhanced when the increase of elastic stiffness of inclusions.
- 388 • Heating was used to accelerate drying kinetics during the second step of drying tests.
389 However, the heating induced cracks were not separated from those induced by drying
390 shrinkage. But as the first observation, the heating enhanced the cracking process due
391 to the difference of thermal expansion between the inclusions and cement paste.

392 In future studies, the thermal expansion induced cracks should be characterized by suit-
393 able experimental methods in order to distinguish them from those induced by the drying
394 shrinkage. Appropriate three dimensional numerical simulations should also be developed
395 for the description of drying shrinkage and heating induced cracking processes.

396 6. Acknowledgements

397 The present work was partially supported by the I-site project Multifrac of University of
398 Lille. The microstructural analysis was realized with the ISIS4D X-Ray CT platform, which
399 has been funded by International Campus on Safety and Intermodality in Transportation
400 (CISIT), the Nord-Pas-de-Calais Region, the European Community and the National Center
401 for Scientific Research. The authors gratefully acknowledge the support of these institutions.

References

- [1] Alam, S. Y., Saliba, J., Loukili, A., 2014. Fracture examination in concrete through combined digital image correlation and acoustic emission techniques. *Construction and Building Materials* 69, 232–242.
- [2] Baant, Z. P., Raftshol, W. J., 1982. Effect of cracking in drying and shrinkage specimens. *Cement and Concrete Research* 12 (2), 209–226.
- [3] Bisschop, J., Van Mier, J., 2002. Effect of aggregates on drying shrinkage microcracking in cement-based composites. *Materials and Structures* 35 (8), 453–461.
- [4] Bisschop, J., Van Mier, J., 2002. How to study drying shrinkage microcracking in cement-based materials using optical and scanning electron microscopy? *Cement and concrete research* 32 (2), 279–287.
- [5] Brooks, R. A., Di Chiro, G., 1976. Beam hardening in x-ray reconstructive tomography. *Physics in medicine & biology* 21 (3), 390.
- [6] Burlion, N., Bernard, D., Chen, D., 2006. X-ray microtomography: application to microstructure analysis of a cementitious material during leaching process. *Cement and Concrete research* 36 (2), 346–357.
- [7] Chen, P.-W., Chung, D., 1995. Effect of polymer addition on the thermal stability and thermal expansion of cement. *Cement and concrete research* 25 (3), 465–469.
- [8] Dezecot, S., Buffiere, J.-Y., Koster, A., Maurel, V., Szymtka, F., Charkaluk, E., Dahdah, N., El Bartali, A., Limodin, N., Witz, J.-F., 2016. In situ 3d characterization of high temperature fatigue damage mechanisms in a cast aluminum alloy using synchrotron x-ray tomography. *Scripta Materialia* 113, 254–258.
- [9] Elaqla, H., Godin, N., Peix, G., R'Mili, M., Fantozzi, G., 2007. Damage evolution analysis in mortar, during compressive loading using acoustic emission and x-ray tomography: Effects of the sand/cement ratio. *Cement and Concrete Research* 37 (5), 703–713.
- [10] Gallucci, E., Scrivener, K., Groso, A., Stampanoni, M., Margaritondo, G., 2007. 3d experimental investigation of the microstructure of cement pastes using synchrotron x-ray microtomography (μ ct). *Cement and Concrete Research* 37 (3), 360–368.
- [11] Goltermann, P., 1995. Mechanical predictions of concrete deterioration; part 2: Classification of crack patterns. *Materials Journal* 92 (1), 58–63.
- [12] Grassl, P., Wong, H. S., Buenfeld, N. R., 2010. Influence of aggregate size and volume fraction on shrinkage induced micro-cracking of concrete and mortar. *Cement and concrete research* 40 (1), 85–93.
- [13] Hammersberg, P., Mångård, M., 1998. Correction for beam hardening artefacts in computerised tomography. *Journal of X-ray Science and Technology* 8 (1), 75–93.
- [14] Hobbs, D., 1974. Influence of aggregate restraint on the shrinkage of concrete. *Journal Proceedings* 71 (9), 445–450.
- [15] Hwang, C.-L., Young, J., 1984. Drying shrinkage of portland cement pastes i. microcracking during drying. *Cement and Concrete Research* 14 (4), 585–594.
- [16] Krissian, K., Westin, C.-F., Kikinis, R., Vosburgh, K. G., 2007. Oriented speckle reducing anisotropic diffusion. *IEEE Transactions on Image Processing* 16 (5), 1412–1424.
- [17] Landis, E. N., Nagy, E. N., 2000. Three-dimensional work of fracture for mortar in compression. *Engineering Fracture Mechanics* 65 (2-3), 223–234.
- [18] Lenoir, N., Bornert, M., Desrues, J., Bésuelle, P., Viggiani, G., 2007. Volumetric digital image correlation applied to x-ray microtomography images from triaxial compression tests on argillaceous rock. *Strain* 43 (3), 193–205.
- [19] Li, L., Jia, Y., Rougelot, T., Burlion, N., 2018. Effects of inclusion stiffness on the cracking of cement-based composites under drying: a numerical study. *European Journal of Environmental and Civil Engineering* 22 (sup1), s246–s268.
- [20] Lu, S., Landis, E., Keane, D., 2006. X-ray microtomographic studies of pore structure and permeability in portland cement concrete. *Materials and structures* 39 (6), 611–620.
- [21] Natalie, L., Thomas, R., Jerome, H., ???? Isis4d - in situ innovative set-ups under x-ray microtomography. isis4d.univ-lille.fr.
- [22] Rougelot, T., Burlion, N., Bernard, D., Skoczylas, F., 2010. About microcracking due to leaching in

- 453 cementitious composites: X-ray microtomography description and numerical approach. *Cement and*
454 *concrete research* 40 (2), 271–283.
- 455 [23] Shiotani, T., Bisschop, J., Van Mier, J., 2003. Temporal and spatial development of drying shrinkage
456 cracking in cement-based materials. *Engineering Fracture Mechanics* 70 (12), 1509–1525.
- 457 [24] Soroka, I., 1993. *Concrete in hot environments*. CRC Press.
- 458 [25] Szczesniak, M., Rougelot, T., Burlion, N., Shao, J.-F., 2013. Compressive strength of cement-based
459 composites: Roles of aggregate diameter and water saturation degree. *Cement and Concrete Composites*
460 37, 249–258.
- 461 [26] Weickert, J., 1998. *Anisotropic diffusion in image processing*. Vol. 1. Teubner Stuttgart.
- 462 [27] Wong, H., Zobel, M., Buenfeld, N., Zimmerman, R., 2009. Influence of the interfacial transition zone
463 and microcracking on the diffusivity, permeability and sorptivity of cement-based materials after drying.
464 *Mag. Concr. Res* 61 (8), 571–589.